Simultaneous increase in electrical conductivity and Seebeck coefficient in highly boron-doped nanocrystalline Si

2013 Nanotechnology 24 205402

(http://iopscience.iop.org/0957-4484/24/20/205402)

Nanotechnology **24** (2013) 205402 (11pp) doi:10.1088/0957-4484/24/20/205402

Simultaneous increase in electrical conductivity and Seebeck coefficient in highly boron-doped nanocrystalline Si

Neophytos Neophytou[1], Xanthippi Zianni[2,3], Hans Kosina[1], Stefano Frabboni[4], Bruno Lorenzi[5] and Dario Narducci[5,6]

[1] Institute for Microelectronics, Technical University of Vienna, Vienna, A-1040, Austria
[2] Department of Applied Sciences, Technological Educational Institution of Chalkida, 34 400 Psachna, Greece
[3] IAMPPNM, Department of Microelectronics, NCSR 'Demokritos', 153 10, Athens, Greece
[4] Department of Physics, University of Modena and Reggio Emilia, via Campi 213/A, I-41100 Modena, Italy
[5] Department of Materials Science, University of Milano–Bicocca, via R. Cozzi 53, I-20125 Milano, Italy
[6] Consorzio DeltaTi Research, Milano, Italy

E-mail: neophytou@iue.tuwien.ac.at

Received 3 January 2013, in final form 28 March 2013
Published 19 April 2013
Online at stacks.iop.org/Nano/24/205402

Abstract
A large thermoelectric power factor in heavily boron-doped p-type nanograined Si with grain sizes ∼30 nm and grain boundary regions of ∼2 nm is reported. The reported power factor is ∼5 times higher than in bulk Si. It originates from the surprising observation that for a specific range of carrier concentrations, the electrical conductivity and Seebeck coefficient increase simultaneously. The two essential ingredients for this observation are nanocrystallinity and extremely high boron doping levels. This experimental finding is interpreted within a theoretical model that considers both electron and phonon transport within the semiclassical Boltzmann approach. It is shown that transport takes place through two phases so that high conductivity is achieved in the grains, and high Seebeck coefficient by the grain boundaries. This together with the drastic reduction in the thermal conductivity due to boundary scattering could lead to a significant increase of the figure of merit ZT. This is one of the rare observations of a simultaneous increase in the electrical conductivity and Seebeck coefficient, resulting in enhanced thermoelectric power factor.

(Some figures may appear in colour only in the online journal)

1. Introduction

The thermoelectric performance of a material is quantified by the dimensionless figure of merit $ZT = \sigma S^2 T/\kappa$, where σ is the electrical conductivity, S is the Seebeck coefficient, and κ is the thermal conductivity. Although traditionally ZT remained low (below one for most materials), over the last years, much larger ZT values were achieved in nanostructures due to a significant reduction in their thermal conductivity [1, 2]. Silicon nanostructures have also been recently proposed as efficient thermoelectric materials due to such a significant reduction in their thermal conductivity compared to bulk Si. Recent experimental measurements in Si nanowires with diameters below 50 nm reported thermal conductivity values as low as $\kappa = 1$–2 W m^{-1} K^{-1}, which resulted in a thermoelectric figure of merit ZT ∼ 1 [3, 4]. This is an impressive increase in ZT with respect to the bulk value $ZT_{bulk} \sim 0.01$. With the reported thermal conductivities approaching the amorphous limit, however, it becomes clear that any further benefits in thermoelectric performance must

come from the power factor σS^2 [5, 6]. In addition, it was shown that low thermal conductivities, while increasing the conversion efficiency, may detrimentally affect the power output of thermoelectric harvesters [7].

Recent experimental works in nanostructures have indeed reported large Seebeck coefficients in a variety of materials such as MnO_2 powders [8], PbTe nanowires [9], oxide nanofibers [10], two-dimensional $SrTiO_3$ electron gas channels [11], heavily-doped Si [12], and materials with impurity resonant levels [13]. In these cases, the increase in the Seebeck coefficient was attributed to the modifications of the density of states around the Fermi level. Another nanostructured geometry in which a significant increase in the Seebeck coefficient was observed is the superlattice geometry for cross-plane transport channels. In this case, the benefits originate from the enhanced energy filtering of hot and cold carriers from the superlattice energy barriers [14]. As of now, however, experimental efforts were not able to achieve a significant relaxation of the adverse interdependence between electrical conductivity and Seebeck coefficient that limits the thermoelectric power factor. Efforts that utilize low dimensional materials for power factor enhancement are not successful to date, despite theoretical predictions [15–18]. Only limited benefits from the electronic power factor were, therefore, observed.

In this work, we present room temperature measurements for the thermoelectric coefficients of heavily boron-doped nanocrystalline Si with grain sizes ∼30 nm. Our data demonstrate that the built-in barriers around the grain boundaries increase the energy filtering and consequently the Seebeck coefficient, as expected [14, 6, 1, 19]. More importantly, however, for certain carrier concentrations, a surprising simultaneous improvement in the electrical conductivity is observed, resulting in a large thermoelectric power factor. This unexpected increase of the power factor in nanocrystalline silicon is related to the precipitation of a second phase around grain boundaries [20–22]. To achieve this unexpected effect, both nanocrystallinity and extremely high doping levels of boron in the grains are essential ingredients.

To interpret the experimental data we perform a theoretical analysis of the thermoelectric performance of nanograined Si by considering both semiclassical electron and phonon transport. We show that for carrier concentrations around $p \sim 5 \times 10^{19}$ cm^{-3}, a formation of a depletion region around the grain boundaries allows the Fermi level to be placed well into the valence band of the grain, but still below the grain boundary barrier, such that simultaneous enhancement of the electrical conductivity and the Seebeck coefficient is achieved. We show that this strong control over the Fermi level placement with doping is possible because in the nanocrystalline structure the contribution of the grain boundary regions is comparable to the contribution of the grain regions, which is not the case in the microcrystalline materials. Finally, we show that with the additional strong reduction in thermal conductivity due to enhanced boundary and defect scattering of phonons, ZT values comparable to the ones reported for monocrystalline Si NWs [3, 4] can potentially be achieved.

2. Experimental method

Films of nanocrystalline silicon (thickness of 200 nm) were deposited onto oxidized Si substrates by chemical vapor deposition and subsequently implanted with boron through an aluminum sacrificial layer with a fluence of 2×10^{16} cm^{-2} at an energy of 60 keV. The total nominal boron density is 4.4×10^{20} cm^{-3}. Implantation damage was recovered by rapid thermal annealing at 1050 °C for 30 s. Samples were then submitted to a sequence of annealing cycles in Ar, carried out at temperatures from 500 to 1000 °C in 100 °C steps, each treatment lasting 2 h. After each annealing step, aluminum contacts were deposited, and electrical resistivity, Hall coefficient and thermopower were measured. Metal pads were removed after measurements by HCl etching prior to the subsequent annealing step.

Samples for the Seebeck and the electrical conductivity measurements were obtained by cutting 50×5 mm^2 rectangular chips and evaporating two aluminum contacts through a shadow mask. For the Hall measurements, 17×17 mm^2 samples were cut and aluminum contacts were evaporated on small areas in the four corners according to the Van der Pauw geometry. Hall measurements were carried out with a maximum magnetic field of 0.5 T. Accuracy was found to be better than ±1%. Seebeck coefficient was measured using a home-built system implementing the integral method [23]. The temperature of the cold contact was kept fixed at 10 °C while the other contact was heated between 40 and 120 °C. Conductivity was determined by current–voltage characteristics at 20 °C. The experimental setup was calibrated towards single-crystal silicon samples of known doping level. Furthermore, each Seebeck coefficient measurement was repeated on the same sample at least three times to ensure data reliability and to evaluate their accuracy. Both charge transport coefficients were also repeated on nominally identical samples and found to be reproducible within ±3%.

As boron density exceeds its solubility in silicon at room temperature, annealing promotes diffusion-limited precipitation of a silicon boride second phase. As a result, the carrier density was found to decrease upon annealing [22]. A quite unexpected concurrent increase of the thermoelectric power and of the conductivity was reported for heat treatments at temperatures above 800 °C. Upon annealing at 1000 °C a power factor of 15 mW K^{-2} m^{-1} (much higher than in p-type bulk Si, or p-type Si nanowires [3, 4]) was measured.

3. Theoretical model

3.1. Electronic transport in uniform materials

The electrical conductivity and Seebeck coefficient within the linearized Boltzmann theory are given by the following expressions [24]:

$$\sigma = q_0^2 \int_{E_0}^{\infty} \mathrm{d}E \left(-\frac{\partial f_0}{\partial E}\right) \Xi(E), \tag{1a}$$

$$S = \frac{q_0 k_\mathrm{B}}{\sigma} \int_{E_0}^{\infty} \mathrm{d}E \left(-\frac{\partial f_0}{\partial E}\right) \Xi(E) \left(\frac{E - E_\mathrm{F}}{k_\mathrm{B} T}\right), \tag{1b}$$

where the transport distribution function $\Xi(E)$ is defined as [17, 24]:

$$\Xi(E) = N(E)\upsilon(E)^2\tau(E) \quad (2a)$$

$$\tau(E) = \frac{\lambda_0(E/k_BT)^r}{\upsilon(E)} \quad (2b)$$

where $\upsilon(E)$ is the band-structure velocity, $\tau(E)$ is the momentum relaxation time, $N(E)$ is the 3D valence band density of states, and λ_0 is the mean-free-path (MFP) for scattering.

In equation (2) the energy dependence of the mean-free-path for scattering is introduced with a characteristic exponent r that defines a specific scattering mechanism. In the case of phonon scattering in 3D channels that is assumed here, the MFP is energy independent [25, 26], $r = 0$, and consequently the scattering rate is proportional to the density of states. For ionized impurity scattering, different expressions for the scattering rate and for the screening length work better for different doping concentrations [26–28]. We use the Brooks–Herring model as described in [26], which works satisfactorily for doping concentrations up to 10^{18} cm^{-3} [27]. Above that (which is more relevant to our data), we use the strongly screened transition rate as described in [26]. We also include the influence of quantum reflections that a series of uniform barriers (at the grain boundaries) will impose, as described in [29]. Although our structures are neither uniform, nor one-dimensional, we include this scattering mechanism as an approximation.

Figure 1(a) shows the MFP versus energy for all scattering mechanisms we employ: acoustic phonons (magenta), acoustic plus optical phonons (red) (still assuming a simplified proportionality of the scattering rate to density of states), quantum reflections (blue), and impurity scattering (green). In black we show the total MFP calculated using Matthiessen's rule. The calculated position of the Fermi level in our nanocrystalline structures for $p = 5.6\times10^{19}$ cm^{-3} is indicated by the dashed line. The dominant scattering mechanism at this doping concentration is ionized impurity scattering, which has a MFP of ∼1 nm and determines the overall MFP. Our simulator is calibrated to the mobility data of bulk Si, see figure 1(b). Our calculated mobility (black line) is in agreement with the measured mobility data for p-type bulk silicon from the works of Jacoboni [30, 31] (black dots) and Masetti [32] (green dots). For this we use $\lambda_0 = 7.4$ nm for phonons. Our results agree particularly well at the carrier concentrations of interest, around $p = 5 \times 10^{19}$ cm^{-3}. By blue dots we denote the mobility measurements for our nanocrystalline structures. Interestingly, the mobility of that material at the lower carrier concentration (at $p = 5.6 \times 10^{19}$ cm^{-3}) is even higher than that of bulk. This can be explained by our model (green line) and will be discussed below.

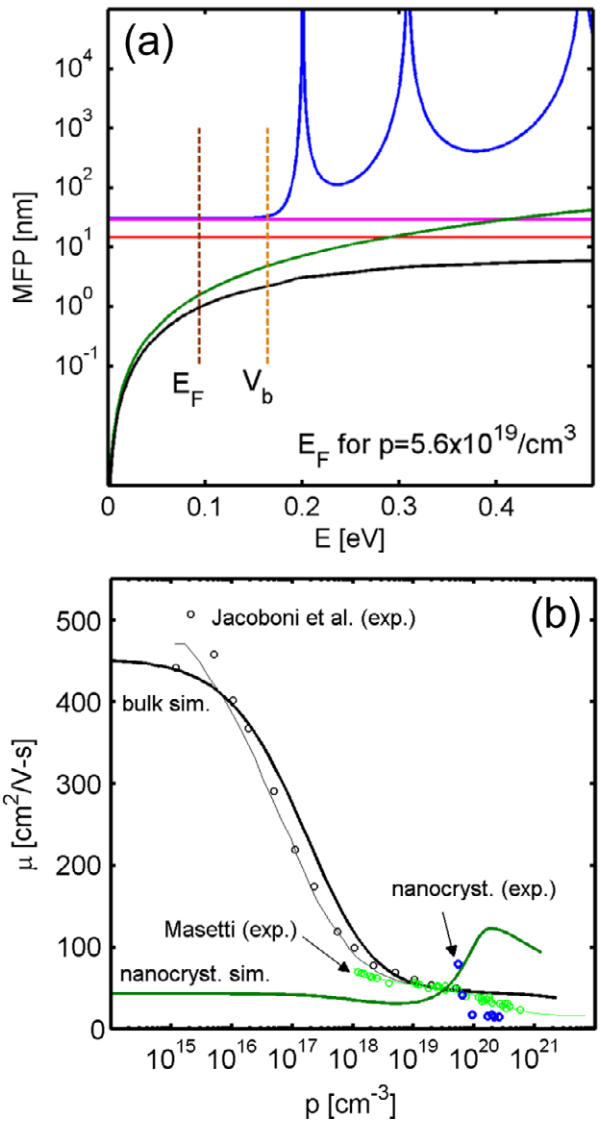

Figure 1. (a) The calculated scattering mean-free-paths (MFPs) of holes versus energy for different scattering mechanisms. (i) Acoustic phonons (magenta). (ii) Acoustic plus optical phonons (red). (iii) Quantum reflections from a series of uniformly spaced barriers of height V_b (blue). (iv) Ionized impurity scattering (green). The overall MFP is shown in black. The position of the Fermi level at $p = 5.6 \times 10^{19}$ cm^{-3} in the nanocrystalline structure analyzed is indicated in brown-dashes. (b) p-type bulk Si mobility measurements from [30] (black dots/thin line fitting), and [32] (green dots/thin line fitting). Simulation results for bulk p-type Si are shown in black. Simulation results for nanograined Si are shown in solid-green. The extracted mobility from our nanograined Si samples is depicted by the blue dots.

3.2. Phonon thermal conductivity

The phonon thermal conductivity is calculated using the kinetic theory within the relaxation time approximation. The thermal conductivity along the transport z-direction is given by the following standard expression [33]:

$$\kappa_z = \sum_k \sum_p k_B x^2 \times \frac{e^x}{V(e^x-1)^2}\upsilon^2(k,p)\tau(k,p)\cos^2[\theta_z(k)] \quad (3)$$

with $x = \hbar\omega(k,p)/k_BT$. In the above equation k is the phonon wavevector, p is the polarization and υ is the group velocity

determined form the slope of the dispersion curves $\upsilon(k, p) = \mathrm{d}\omega(k, p)/\mathrm{d}k$, ω is the phonon frequency, $\tau(k, p)$ is the phonon relaxation time due to scattering, $\theta_z(k)$ is the angle between the wavevector k and the direction z, and V is the volume of the grain.

We used bulk phonon dispersion and relaxation times, assumptions previously validated for Si nanowires and nanofilms [34]. The phonon scattering relaxation time $\tau(k, p)$ is obtained by Matthiessen's rule, expressing that the inverse of the total relaxation time is the sum of the inverse of the relaxation times due to the contributions of the individual scattering mechanisms:

$$\frac{1}{\tau} = \frac{1}{\tau_{\mathrm{U}}} + \frac{1}{\tau_{\mathrm{d}}} + \frac{1}{\tau_{\mathrm{BC}}}. \tag{4}$$

We consider scattering due to Umklapp processes, phonon–defect interactions, and boundary scattering. The relaxation time due to Umklapp processes is given by:

$$\frac{1}{\tau_{\mathrm{U}}} = A\omega^{\chi} T^{\xi} \mathrm{e}^{-B/T}. \tag{5a}$$

The relaxation time due to phonon–defect interactions is given by:

$$\frac{1}{\tau_{\mathrm{d}}} = D\omega^4 \tag{5b}$$

where A, B, D, χ and ξ are determined to match the variation of the experimental thermal conductivity of bulk Si from [34]. The boundary scattering relaxation time is:

$$\frac{1}{\tau_{\mathrm{BC}}} = \upsilon(k, p)/[FL(k)] \tag{5c}$$

where $L(k)$ is the distance a phonon can travel between two surfaces [35]. The boundary scattering is treated beyond the commonly used phenomenological model in the Casimir limit where the boundary scattering MFP would be approximated by the width of the nanograin. Here, the distance $L(k)$ that a phonon can travel between two surfaces is calculated for each wavevector and phonon polarization, and an average MFP over the grain is calculated. F depends on the root-men-square (rms) value of the boundary roughness, n, though the specularity parameter β, and is given by the following expression:

$$F = \left(\frac{1 + \beta(k)}{1 - \beta(k)}\right) \tag{6}$$

where $\beta(k) = \mathrm{e}^{-4k^2n^2}$. The values of β vary from 1 (for specular boundary scattering) to 0 (for completely diffusive boundary scattering). The value of η was calibrated after interpreting experimental data for temperature dependence of the Si nanowires of [36]. It turns out that $n = 0.3$ nm explains the Si nanowire data adequately. With this value, our model provides thermal conductivity values for the grains we consider in good agreement with the grain thermal conductivity values reported in the work of [37] as well.

To calculate the thermal conductivity of the nanocrystalline structure we assume that the average grain can be represented by a rectangular grain of length L_{G} and width d. The calculated thermal conductivity of the nanograin is in agreement with other works [37]. In this work, we assume that the concentration of defects and impurities is higher in the grain boundaries where the thermal conductivity κ_{GB} is assumed to be close to the amorphous limit. The overall phonon thermal conductivity κ_{l} can be estimated from [38]:

$$\frac{v_{\mathrm{tot}}}{\kappa_{\mathrm{l}}} = \frac{v_{\mathrm{G}}}{\kappa_{\mathrm{G}}} + \frac{v_{\mathrm{GB}}}{\kappa_{\mathrm{GB}}} \tag{7}$$

where $v_{\mathrm{tot}} = v_{\mathrm{G}} + v_{\mathrm{GB}}$, and v_{G} and v_{GB} are the volumes of the grain regions and the grain boundary regions, respectively (idealized as rectangular regions [39]).

3.3. Thermoelectric coefficients of nanocrystalline material

For the electronic transport calculation in the nanocrystalline material we follow the usual formalism that describes transport in polycrystalline materials. We assume a sequence of grains of length L_{G}, separated by rectangular grain boundary barriers of width L_{GB}, as shown in figure 2(b). Transport is limited by the barriers of the grain boundaries and shows thermally activated behavior [39–41]. This resembles a 1D channel, but the main findings provide qualitative insight into the operation of 3D bulk nanocrystalline as well, since often such simplified models tend to describe their properties adequately [39]. The effective barrier height seen by charge carriers can be extracted from the data of mobility versus inverse temperature. A logarithmic plot of μ versus $1/T$ is shown in figure 2(a). From the slope of the linear part at high temperatures (left side) the barrier is extracted to be $V_{\mathrm{b\ eff}} = 0.07$ eV. In reality, the energy band of a polycrystalline material looks more like the one depicted in the inset of figure 2(a), where a depletion region forms around the grain boundaries and extends into the grain region [39, 40]. In our case we simplify the description of the band diagram by extending the depletion region into the grain and increase V_{b} in a rectangular manner as shown in figure 2(c). When describing a structure, therefore, the inputs to our model are the barrier height V_{b} and the percentage of mobile charge that the grain is depleted from. It should be noted that direct measurement of the trap concentration, which can be carried out in microcrystalline materials using for instance light beam induced current spectroscopy [42], gets almost impossible in nanocrystalline systems. Therefore, using V_{b} and the channel depletion ratio as model parameters comes out as the only viable options.

The composite electrical conductivity can be estimated by [38]:

$$\frac{v_{\mathrm{tot}}}{\sigma_{\mathrm{tot}}} = \frac{v_{\mathrm{G}}}{\sigma_{\mathrm{G}}} + \frac{v_{\mathrm{GB}}}{\sigma_{\mathrm{GB}}}. \tag{8}$$

The electrical conductivity in the grain boundary region is given by:

$$\sigma_{\mathrm{GB}}(E) = 0 \qquad \text{for } E \geq V_{\mathrm{b}} \tag{9a}$$

$$\sigma_{\mathrm{GB}}(E) = \sigma_{\mathrm{G}}^{0}(E) T_{\mathrm{WKB}}(E) \qquad \text{for } E > V_{\mathrm{b}}. \tag{9b}$$

The model assumes that there is a barrier built on the amorphous grain boundary region, and transport is thermionic

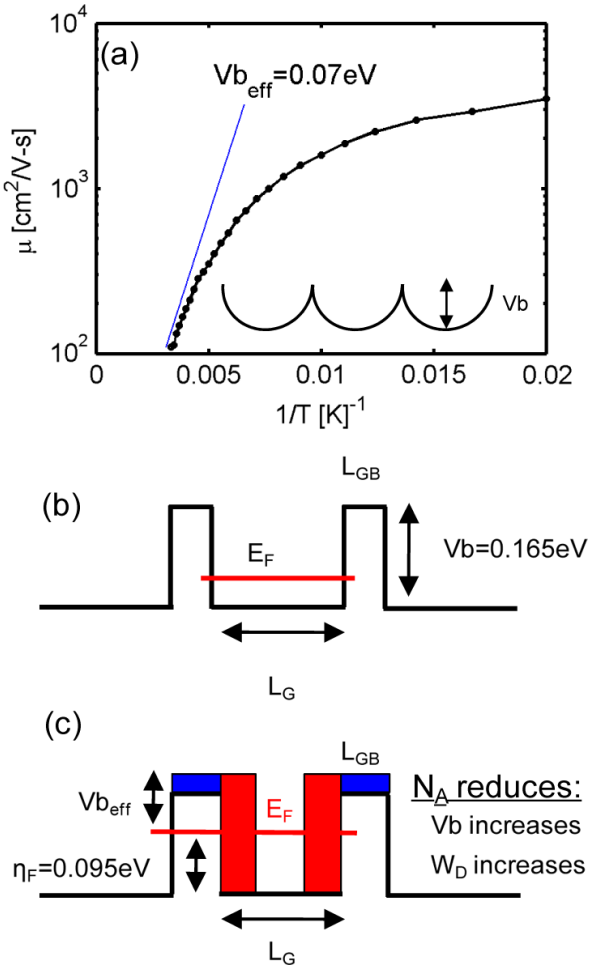

Figure 2. (a) The μ versus T^{-1} experimental measurements. An effective barrier height of $V_{\text{b eff}} = 0.07$ eV is extracted. Inset: an illustration of the band profile in the poly-Si material, indicating the barrier increase at the position of the grain boundaries and the depletion region extending into the grain (see [39]). (b) The nanocrystalline model, consistent of grain and grain boundaries. L_G is the length of the grain region and L_{GB} the length of the grain boundary region. (c) The simplified nanocrystalline model including the depletion region effect. The depletion region extends into the grain and the barrier increases. At 45% grain depletion, the Fermi level is positioned 0.095 eV into the valence band.

over that barrier. Any effects occurring at the interface could be lamped into the value of σ^0_{GB}, and effectively included as an additional series resistance. In this work however, we assumed that $\sigma^0_{GB}(E) = \sigma^0_G(E)$, but include the effect of quantum mechanical reflections that can occur over the barrier using the transmission $T_{WKB}(E)$ given by the WKB approximation.

The Seebeck coefficient is determined by the combined transport in the grains and in the grain boundaries of the nanocrystalline material. There are two regimes of transport as described in [43] and recently in [44]: (i) when carriers flow ballistically (with negligible energy relaxation) in the grain until they reach the grain boundary, and (ii) when carrier transport in the grains is diffusive (energy relaxation of carriers prevails). In the first case, the overall Seebeck coefficient is determined by the Seebeck coefficient of the highest barrier, which is the barrier introduced by the grain boundaries.

$$S_{\text{ball}} = S_{GB}. \tag{10a}$$

Note that we use the term ballistic, referring to the carrier energy, although the carrier momentum is strongly relaxed. In the second case, the Seebeck coefficient is determined by the weighted average of the Seebeck coefficients of the two regions, with the weighting factor being the temperature drop in each region, which is determined by their thermal conductivities [38, 44]:

$$S_{\text{diff}} = \frac{S_G \Delta T_G + S_{GB} \Delta T_{GB}}{\Delta T_G + \Delta T_{GB}} = \frac{S_G v_G/\kappa_G + S_{GB} v_{GB}/\kappa_{GB}}{v_G/\kappa_G + v_{GB}/\kappa_{GB}}. \tag{10b}$$

In the case where transport is neither fully ballistic, nor fully diffusive, we approximate the overall Seebeck coefficient by weighting the two quantities from equations (10*a*) to (10*b*). The weighting factor is the fraction of energy relaxation in the grain, determined by the MFP of the energy relaxing processes (λ_E), here optical phonons [43–45]. As in the case of estimating the ballisticity of transistor channels, this is given by $C = \lambda_E/(\lambda_E + L_G)$ [45]. For grain lengths $L_G \sim 30$ nm, which are about what is observed in the TEM images of our structures, C is computed to be $C \sim 0.5$. We note that this is a simple estimate of the average energy relaxation in the grain, although in principle this quantity has a spatial dependence as well. The overall Seebeck coefficient is then given by:

$$S_{\text{tot}} = C S_{\text{ball}} + (1 - C) S_{\text{diff}}. \tag{11}$$

Finally, the ZT figure of merit is computed by the relation $ZT = \sigma S^2 T/\kappa_l$.

4. Thermoelectric performance

In figure 3 we present in blue dots the measured data for the nanocrystalline structures versus carrier density. Figure 3(a) shows the electrical conductivity, figure 3(b) the Seebeck coefficient, and figure 3(c) the power factor. During the sequential annealing steps, the amount of boron segregating at the grain boundaries decreases (dose loss through out-diffusion of boron), and the barrier heights and the width of the depletion region around the grain boundaries increase (decreasing the overall mobile carrier concentration by almost an order of magnitude from $p = 4.4 \times 10^{20}$ to 5.6×10^{19} cm^{-3}), as also described by Seto and Orton [39, 40]. The data from right to left (for reducing carrier density) show the evolution of the thermoelectric coefficients, measured at room temperature, after the sequential annealing steps. The left-most point corresponds to the structure under the largest number of annealing steps, and the largest annealing temperature, 1000 °C. In the direction of decreasing concentration (right to left), the data shows that the conductivity initially drops from $\sigma_{\text{init.}} = 600\ \Omega^{-1}$ cm^{-1} to $\sigma = 265\ \Omega^{-1}$ cm^{-1}. Below concentrations $p = 10^{20}$ cm^{-3}, however, it increases to $\sigma_{\text{final}} = 710\ \Omega^{-1}$ cm^{-1}. The Seebeck coefficient, on the other hand, monotonically increases from

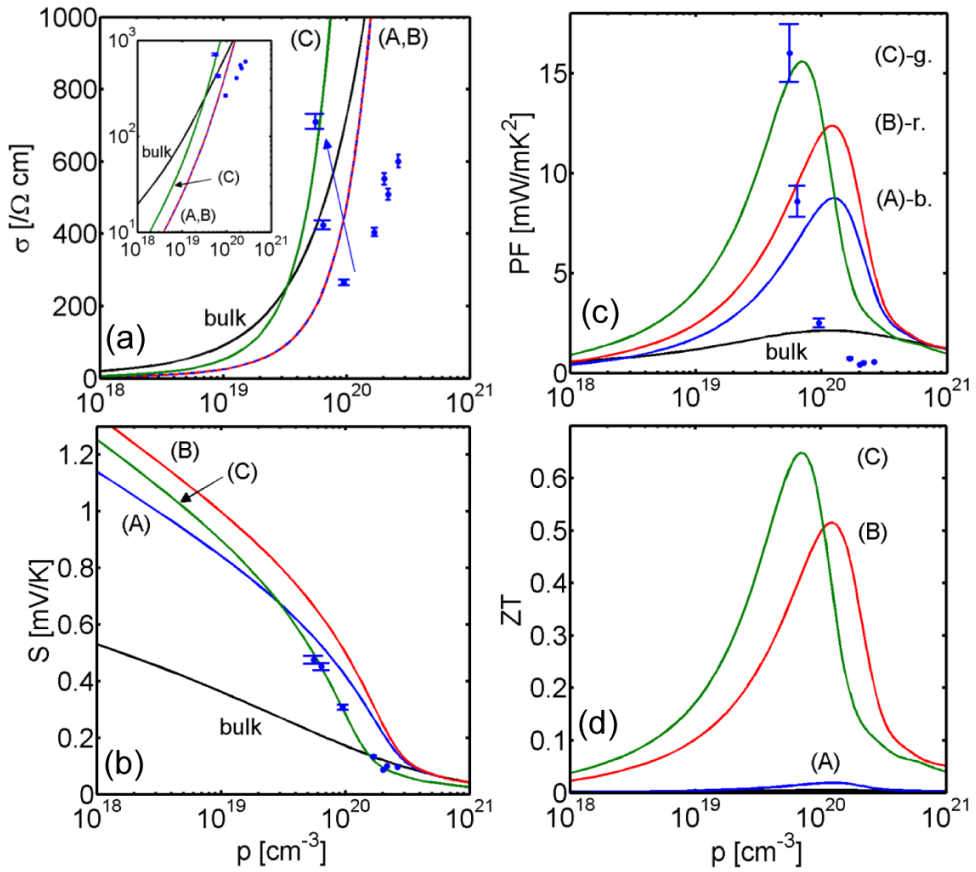

Figure 3. Thermoelectric coefficients versus carrier concentration for: (I) measurements for the nanocrystalline Si material (blue dots), (II) simulation results for p-type bulk Si (black lines), and (III) simulations of nanocrystalline Si with grain size $L_G = 30$ nm, grain boundary width $L_{GB} = 2$ nm, and barrier height $V_b = 0.165$ eV (blue, red, green lines). Specific considerations: (i) assume $\kappa_l = 140$ W m^{-1} K^{-1} in the entire material (blue lines). (ii) Assume a non-uniform thermal conductivity with $\kappa_G = 12$ W m^{-1} K^{-1} and $\kappa_{GB} = 2$ W m^{-1} K^{-1} (red lines). (iii) Same as (ii) but in addition the depletion width is such that that reduces the carrier concentration in the grain to 55% (green lines). This is the model case for the left-most experimental point. (a) The electrical conductivity. Inset: the electrical conductivity in logarithmic scale. (b) The Seebeck coefficient. (c) The power factor. (d) The ZT figure of merit.

$S_{init.} = 0.1 \times 10^{-3}$ V K^{-1} to $S_{final} = 0.48 \times 10^{-3}$ V K^{-1}. For carrier concentrations below $p = 10^{20}$ cm^{-3}, where both σ and S increase, the σS^2 largely increases (from $\sigma S^2_{init.} = 0.55 \times 10^{-3}$ W m^{-1} K^{-2} to $\sigma S^2_{final} = 15.7 \times 10^{-3}$ W m^{-1} K^{-2}). Below we provide explanations for this behavior using our theoretical model.

In our calculations we keep the grain size constant at $L_G = 30$ nm and the width of the grain boundary at $L_{GB} = 2$ nm, consistent with what is observed in the TEM images of our samples [21]. (Note that in the depth direction the distribution of grain is more elongated with $W_G = 100$ nm, which has some effect on our calculations as well, as we discuss below.) To identify the influence of each parameter that affects the performance of the nanocrystalline material, we simulate structures with different features. Starting from the p-type bulk Si calculation (black line), we gradually add: (i) the grain boundaries with barriers $V_b = 0.165$ eV (blue line), (ii) a reduction (from bulk) and variation in the thermal conductivity of the grain with respect to the grain boundary region with $\kappa_G = 12$ W m^{-1} K^{-1} and $\kappa_{GB} = 2$ W m^{-1} K^{-1} (red line), (iii) an increase of the depletion width in the grain region (green line) that leaves only 55% of the grain non-depleted. Our simulations aimed to interpret the left-most measurement points shown in figure 3, which correspond to the highest annealing temperature (1000 °C) and the lowest hole concentration. At such high annealing temperature, an effective average barrier is formed for carrier transport. Our data shows that this is not the case for lower annealing temperatures. The value $V_b = 0.165$ eV provides a good match between simulation and measurements for both Seebeck coefficient and electrical conductivity. Note that this value is also consistent with the experimental data on the temperature dependence of the mobility, from which we have extracted an effective barrier height of $V_{b\,eff} \sim 0.07$ eV (figure 2(a)). In the material with the highest power factor, the position of the Fermi level at an overall carrier concentration $p = 5.6 \times 10^{19}$ cm^{-3} is ~0.095 eV into the valance band (figure 2(c)). This results in an overall barrier of $V_b = 0.165$ eV.

4.1. Introduction of grain boundaries (blue lines—labeled (A) in figure 3)

With the introduction of the grain boundary barriers the most drastic effects are observed in the Seebeck coefficient

in figure 3(b) (blue line), since the barriers increase carrier filtering. Indeed, after the sequential annealing steps that build these barriers, the measured data show that the Seebeck coefficient increases from $S_{\text{init.}} = 0.1$ V K^{-1} at carrier concentrations $p = 4.4 \times 10^{20}$ cm^{-3}, to $S_{\text{final}} = 0.48 \times 10^{-3}$ V K^{-1} at $p = 5.6 \times 10^{19}$ cm^{-3}. This is captured adequately by our model (blue line labeled (A) in figure 3(b)), which shows the Seebeck coefficient versus carrier concentration for $V_b = 0.165$ eV. The barriers, on the other hand, reduce the electrical conductivity since only high energy carriers can overpass them. The measurements show that the conductivity is reduced from $\sigma_{\text{init.}} = 600\ \Omega^{-1}$ cm^{-1} (at $p = 4.4 \times 10^{20}$ cm^{-3}) to $\sigma = 265\ \Omega^{-1}$ cm^{-1} (at $p = 1 \times 10^{20}$ cm^{-3}) as the barriers are built. Indeed, our calculations for such a material with barriers of $V_b = 0.165$ eV show a reduction in conductivity compared to bulk (black line in figure 3(a)) at low carrier concentrations since carriers do not have enough energy to overpass the barriers (blue–red line labeled (A, B) in figure 3(a) and in the inset of figure 3(a)). At higher carrier concentrations, however, the Fermi level in the channel is high enough, and the carriers have enough energy to surmount the barriers. The conductivity then sharply increases as indicated in figure 3(a) (blue–red line), reaching the monocrystalline material conductivity at concentrations above $p \sim 10^{20}$ cm^{-3}. As a consequence of the increase in S and only weak reduction in σ at high concentrations, the power factor $S^2\sigma$ increases as shown in figure 3(c) compared to bulk (blue-(A) versus black line). The maximum power factor reaches $\sigma S^2 \sim 9$ mW m^{-1} K^{-2} at concentrations $p \sim 10^{20}$ cm^{-3}, still, however, lower than the maximum measured value of $\sigma S^2 \sim 16$ mW m^{-1} K^{-2}.

4.2. Variation in thermal conductivity (red lines—labeled (B) in figure 3)

In nanograined materials the thermal conductivity decreases drastically with decreasing grain size due to confinement and strong phonon boundary scattering (see inset of figure 5). A grain of size $30 \times 30 \times 100$ nm^3 (the grain size in this work) was calculated to have thermal conductivity as low as $\kappa_G = 12$ W m^{-1} K^{-1}. Within the grain boundaries phonons are scattered even more strongly by the higher concentration of defects and imperfections and the thermal conductivity can approach the amorphous limit $\kappa_{GB} = 2$ W m^{-1} K^{-1}. The overall thermal conductivity of our structure could then drop below 5 W m^{-1} K^{-1}. According to equation (10*b*), the Seebeck coefficients are weighted by the temperature drops in the different regions, and thus the Seebeck coefficient in the regions with low thermal conductivity is dominant. Therefore, the smaller thermal conductivity of the grain boundaries (where Seebeck is larger) further improves the overall Seebeck coefficient (red line in figure 3(b)) [38, 44]. The electrical conductivity in figure 3(a) is not affected (red and blue lines coincide). As a result, a noticeable improvement can be observed in the power factor in figure 3(c) (red line—(B) versus blue line—(A)). The maximum simulated power factor reaches $\sigma S^2 \sim 12 \times 10^{-3}$ W m^{-1} K^{-2} at concentrations $p \sim 10^{20}$ cm^{-3}, one step closer to the maximum measured value (left-most data point).

4.3. Increase in the width of the depletion region (green lines—labeled (C) in figure 3)

The third effect we consider is the depletion of carriers from the regions near the grain boundary and the increase in the width of the depletion region as the carrier concentration is reduced. This is a normal behavior in polycrystalline Si [39, 40]. The effect is depicted in the simplified schematic of figure 2(c) (the actual shape is as in the inset of figure 2(a)).

In our case, we assume that the grains are partially depleted by 45% (55% non-depleted). Our calculations show that in such case the electrical conductivity in the grain and in the overall structure at lower carrier concentrations (below $p = 3 \times 10^{19}$ cm^{-3}) increases compared to the non-depleted case, but it is still lower than bulk, as shown in figure 3(a) and its inset (green line). We note that we have no way of determining the depletion scale, we rather use it as a parameter to match the measured conductivity. An interesting observation lies in the fact that for concentrations above $p = 3 \times 10^{19}$ cm^{-3}, the electrical conductivity of the nanocrystalline material largely increases, and overpasses that of the monocrystalline bulk. The reason is that at the same carrier (or doping) concentration, the Fermi level resides higher in the grains of the nanocrystalline material compared to the monocrystalline material. The barriers and depletion introduce regions of low carrier concentration. This local reduction is compensated by a rise of the Fermi level within the grain, which consequently causes an increase in the conductivity. Simply stated, there is less space now in the grain to be filled with carriers and the Fermi level rises to maintain global charge neutrality. (We clarify that the carrier concentrations we mention throughout the paper are calculated by assuming a uniformly doped structure. In the non-uniformly doped nanocrystalline material, the doping level is actually higher in the middle of the grain, and lower near and around the grain boundaries.)

The difference between the Fermi level and the band edge in the grain $\eta_F = E_F - E_V$ versus carrier concentration is shown in figure 4(a). η_F is larger (more negative) in the structure that includes barriers (red line), and even higher in the structure that includes depletion, compared to bulk (black line). At carrier concentrations of $p \sim 5.6 \times 10^{19}$ cm^{-3}, η_F is almost $2k_BT$ higher compared to bulk material (black line), and $1.5k_BT$ higher than what it is in the non-depleted grain case (red line). The higher E_F increases the mean-free-path for scattering by almost three times as shown in figure 4(b). As a result, the electrical conductivity in the grain and in the overall structure also increases, as shown in figure 3(a) (green line). Although it slightly reduces the Seebeck coefficient as shown in figure 3(b), it finally improves the power factor by an additional 25% (green line in figure 3(c)), reaching the maximum power factor measured in our samples, which is $\sigma S^2 \sim 15.7 \times 10^{-3}$ W m^{-1} K^{-2}.

4.3.1. Simultaneous increase in σ and S. The simultaneous increase in σ and S can normally not be achieved in thermoelectric materials, and we believe that we demonstrate a rare case in which this happens. It is actually commonly

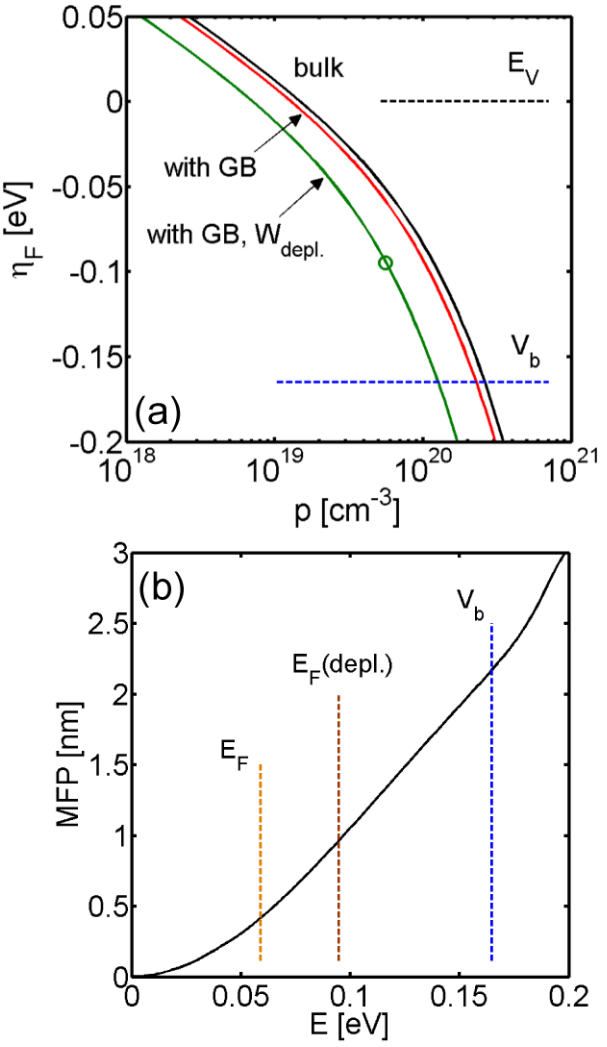

Figure 4. (a) The distance of the Fermi level from the band edge, $\eta_F = E_V - E_F$, versus carrier concentration. Shown: (i) p-type bulk Si (black line), (ii) nanocrystalline Si with grain size $L_G = 30$ nm, grain boundary width $L_{GB} = 2$ nm, and barrier height $V_b = 0.165$ eV (red line), (iii) same as (ii) plus the depletion width is such that it reduces the carrier concentration in the grain to 55% (green line). The energy position of the grain boundary barrier $V_b = 0.165$ eV is indicated by the blue line and the position of the valence band in dashed-black. The green dot at $\eta_F = -0.095$ eV indicates the Fermi level at the carrier concentration of $p = 5.6 \times 10^{19}$ cm^{-3}, where the maximum power factor is achieved. (b) The mean-free-path for scattering versus energy in the grains of the material. The positions of the barrier, and of the Fermi level for cases (ii) and (iii) are indicated.

believed that in no way both the Seebeck coefficient and the electrical conductivity may increase simultaneously with carrier density. This interdependence holds in bulk and can break down in more complex structures where additional mechanisms may modify the dependences of σ and S upon the carrier concentration [12]. In highly doped poly-Si, the boron atoms diffuse easily with increasing annealing temperature, and move towards the grain boundaries where they partially precipitate. The overall carrier concentration, therefore, decreases (the dots move from right to left in figure 3). The formation of dopant clusters at the grain boundaries creates a non-uniform impurity and defect concentration in the material, which increases the barrier heights in the grain boundaries, allows the depletion regions to extend in the grains, and increases the number of scattering centers for phonons in the grain boundary.

We propose that the concurrent increase of the Seebeck coefficient and the electrical conductivity results from the fact that as the barrier rises and/or the width of the depletion region around the grain boundary increases, two effects take place: (i) the Fermi level rises, and is placed well inside the valence band, which allows the faster high energy carriers to participate in transport, and (ii) the overall MFP for scattering increases because high energy carriers are scattered less by impurities, which is the dominant scattering mechanism. These two effects compensate the detrimental effect of the grain boundary barriers on the conductivity, and for $p < 10^{20}$ cm^{-3} (or above a specific E_F position), an overall increase in σ is achieved. The rise in E_F is possible because the volume (or length) of the grain boundary together with the depletion region are comparable to the volume of the ~30 nm grain. For larger grain sizes, i.e. 1 μm, where the grain boundary and depletion region occupy a very small portion of the overall volume, our simulations show that σS^2 approaches the bulk value within <10%. Therefore, both, nanocrystallinity, and extremely high boron doping levels at the center of the grain, are essential ingredients for this novel observation.

4.3.2. ZT figure of merit and thermal conductivity. The calculated ZT figure of merit is shown in figure 3(d) for the three design steps described above: (A) the introduction of grain boundaries (blue line), (B) the variation in the thermal conductivity between the grain and grain boundary (red line), and (C) the charge carrier depletion of the grain region (green line). In case (A), the ZT remains low (blue line) since at this stage of the calculation we have still used the large bulk value for the thermal conductivity, $\kappa_l = 140$ W m^{-1} K^{-1}. An increase in the simulated ZT figure of merit is observed with $ZT_{max} \sim 0.5$ in case (B) (red line) in which the calculated thermal conductivity is significantly lower, $\kappa_l = 12$ W m^{-1} K^{-1} in the grain and $\kappa_l = 2$ W m^{-1} K^{-1} in the amorphous grain boundary regions. In case (C), in which a higher power factor was achieved, the ZT reaches $ZT_{max} \sim 0.65$. We note that similarly high ZT values have been previously observed for monocrystalline 1D Si NWs [3, 4] with much lower thermal conductivities, but here we show that this could be possible in a 3D Si-based material as well. In this material, the contribution originates from both power factor increase, and thermal conductivity reduction.

We mention, however, that in the calculation of the ZT in figure 3(d), we used our calculated thermal conductivity values, since we do not have access to experimentally measured ones. In our measurements we only have access to the cross-plane thermal conductivity, normal to the direction of charged carrier transport, and not in parallel to that [46]. Silicon itself is not expected to be anisotropic—but the morphology is oriented, as in most CVD films. In the film the grains are quite elongated, with the 30 nm size in the in-plane directions and somewhat larger (even up

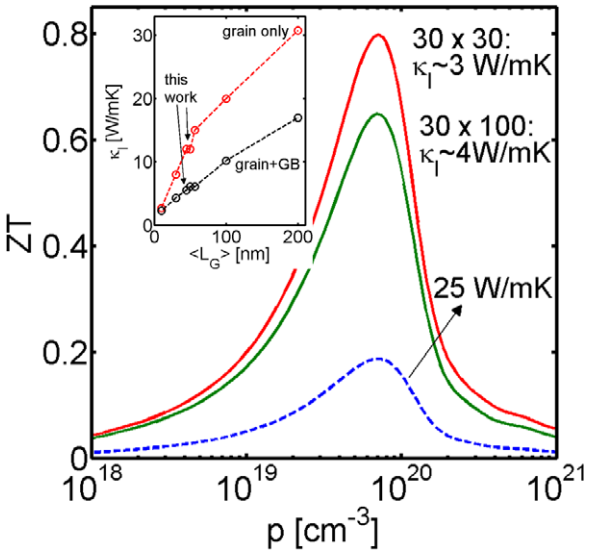

Figure 5. The ZT figure of merit versus carrier concentration for cases: (i) cubic grains of side size 30 nm (red line) and overall thermal conductivity $\kappa_l = 3$ W m^{-1} K^{-1}. (ii) Grain sizes of $30 \times 30 \times 100$ nm^3 (green line—same as in figure 3) and overall thermal conductivity $\kappa_l = 4$ W m^{-1} K^{-1}. (iii) Grain sizes of $30 \times 30 \times 100$ nm^3 with assumed overall thermal conductivity $\kappa_l = 25$ W m^{-1} K^{-1}. Inset: the calculated thermal conductivity as a function of the effective grain size. Red-dashed is the thermal conductivity of the grain only. Black-dashed is the overall thermal conductivity calculated using equation (7) and assuming $\kappa_{GB} = 2$ W m^{-1} K^{-1}.

to ∼100 nm) in the normal-to-the-substrate direction. The thermal conductivity was measured normal to the film by using time-domain thermoreflectance in a previous work [46]. That measured value is $\kappa_{l\,exp.} = 25 \pm 5$ W m^{-1} K^{-1} and was measured both in the as-grown film and after annealing at 1000 °C [46]. Such a value is lower by about a factor five with respect to single-crystal silicon and comparable to the thermal conductivity reported on micro- and nanocrystalline silicon, but higher than our calculations. We believe that the reasons of this discrepancy are: (i) the measurements were performed in the direction where the grain size is of order 100 nm. In that direction, higher conductivities are expected compared to the transport direction in which the grain size is about 30 nm. (ii) We assumed the grain boundary to be an amorphous region with $\kappa_l = 2$ W m^{-1} K^{-1}, which could be an underestimation. (iii) The actual structure contains a distribution of sizes, embedded with a conducting network that also conducts in parallel and not only in series as assumed. These can strongly influence the thermal conductivity and could provide higher measured values than our calculations. Although in the case of electrical transport we had access to several parameters other than the geometry to calibrate our model (concentration, Seebeck, conductivity, barrier heights), in the case of thermal conductivity this was not the case. Therefore, for consistency with the transport orientations, we used our calculated κ_l values for the $30 \times 30 \times 100$ nm^3 grains (with transport along the 30 nm side) in calculating the ZT figure of merit. We would expect that this might provide ZT values closer to the upper limit for such geometry. In this work we mainly focus in identifying the essential physics behind the co-occurrence of improvements in Seebeck coefficient and electrical conductivity, and the exact value of κ_l does not qualitatively affect this.

We finally note that the thermal conductivity measurements showed no change of the thermal conductivity upon annealing, its value being unchanged at 25 ± 5 W K^{-1} m^{-1}. Phonon scattering is seemingly dominated by grain boundaries and is rather insensitive to the formation of an inter-phase around it. Therefore, the improvement of the power factor upon annealing is not compensated by the thermal conductivity reduction in this material. This allows for both the thermal conductivity reduction and the power factor increase to contribute to the ZT improvement.

4.3.3. Approximations and assumptions. In our simulations transport is treated within the semiclassical approximation and the bulk Si bandstructure is used; the potential energy profile is assumed flat within the grains while the width of the depletion region near the boundary is set as a parameter. Two-phase transport is treated within a nanocrystalline material, assuming that carriers travel through a uniform sequence of grains overcoming rectangular potential barriers at the grain boundaries. These simplifications are commonly used to describe transport properties in polycrystalline materials. Although a more sophisticated model could provide quantitatively more reliable estimations, as well as include more geometry details such as the grain size distribution and network conductivity, we do not expect our main qualitative conclusions to be affected. In our approach, we have systematically evaluated the effect of each mechanism and we have identified the major mechanisms that are responsible for the simultaneous increase of the conductivity and the Seebeck coefficient. We emphasize that the experimental data on the mobility, the conductivity, and the Seebeck are simultaneously and consistently interpreted.

Regarding the thermal conductivity calculations, we again assumed an amorphous grain boundary region, and a uniform resistive network for transport. The inset of figure 5 shows the individual grain thermal conductivity as a function of the effective grain sizes, calculated using the geometric ratio of its actual sizes (red-dashed line). The thermal conductivity of a rather large 200 nm diameter grain was found to be $\kappa_l \sim 31$ W m^{-1} K^{-1}, whereas that of a 10 nm grain $\kappa_l \sim 2.7$ W m^{-1} K^{-1}. For the grains under consideration ($30 \times 30 \times 100$ nm^3), $\kappa_l \sim 12$ W m^{-1} K^{-1}. The black-dashed line shows using equation (7) that if $\kappa_{GB} = 2$ W m^{-1} K^{-1}, i.e. amorphous region, the overall thermal conductivity of our structure could drop below 5 W m^{-1} K^{-1}. Our calculations are in agreement with other calculations as well [37]. Our calculated values used in the simulations are smaller than $\kappa_{l\,exp.} = 25 \pm 5$ W m^{-1} K^{-1}. A one-to-one comparison between the theoretically estimated thermal conductivity of the grains/grain boundaries and the measured thermal conductivity normal to the film direction is not possible, as explained above. Nevertheless, in figure 5 we calculate the ZT figure of merit that could be achieved in case (C) of figure 3, once a larger, isotropic $\kappa_{l\,exp.} = 25 \pm 5$ W m^{-1} K^{-1}

is considered. This is shown by the dashed-blue line. The ZT of course now is lower, ZT $\sim$ 0.2, only $\sim$20 times higher than bulk. For comparison purposes we show in green line the same result as in figure 3(d) (C), which stands three times higher. We show, however that once smaller grains are considered, the ZT rises by 20% to ZT $\sim$ 0.8. The first case is the worst case scenario for ZT, since we expect the thermal conductivity to be higher along the longer 100 nm grain dimensions. The last two cases (green and red lines) represent the more optimistic, closer to an upper limit scenario. Still, however, even in the first case, both the thermal conductivity reduction and the power factor increase contribute equally to this ZT improvement.

5. Conclusions

In summary, we report on the thermoelectric power factor of heavily boron-doped nanocrystalline Si material of grain sizes $\sim$30 nm as the carrier concentration drops from $\sim 4.4 \times 10^{20}$ cm^{-3} down to $\sim 5.6 \times 10^{19}$ cm^{-3} upon subsequent annealing steps. Our measurements indicate that the Seebeck coefficient monotonically increases with reduction in the carrier concentration. Interestingly, for carrier concentrations below 10^{20} cm^{-3}, a simultaneous increase in the electrical conductivity is also observed, which provides large power factors, five times larger than what can be achieved in bulk Si. Our theoretical investigation, involving both electron and phonon transport in nanocrystalline Si materials reveals that: (i) the improvement in the Seebeck coefficient can be attributed to the increase in carrier filtering due to the energy barriers at the grain boundaries, and due to the non-uniformity of the lattice thermal conductivity between the grains and grain boundaries. (ii) The improvement in the electrical conductivity is a result of a higher Fermi level in the grain compared to bulk material at the same carrier concentration. This allows high energy carriers to contribute to transport, increases the mean-free-path due to impurity scattering, and thus increases the conductivity in the grain. Our calculations indicate ZT $\sim$ 0.65 could be achieved in the grown polycrystalline films. We finally point out that ZT values well above unity could be possible in such Si nanocrystalline structures of lower dimensionality (thin layers, nanowires) where the thermal conductivity is expected to be further reduced. Our results importantly demonstrate that in the presence of both, nanocrystallinity, and very high doping levels in the crystal grains, the adverse interdependence between the Seebeck coefficient and the electrical conductivity is lifted, resulting in a very high power factor.

References

[1] Venkatasubramanian R, Siivola E, Colpitts T and O'Quinn B 2001 Thin-film thermoelectric devices with high room-temperature figures of merit *Nature* **413** 597–602

[2] Zhao L D *et al* 2011 High performance thermoelectrics from earth-abundant materials: enhanced figure of merit in PbS by second phase nanostructures *J. Am. Chem. Soc.* **133** 20476–87

[3] Boukai A I, Bunimovich Y, Tahir-Kheli J, Yu J-K, Goddard W A III and Heath J R 2008 Silicon nanowires as efficient thermoelectric materials *Nature* **451** 168–71

[4] Hochbaum A I, Chen R, Delgado R D, Liang W, Garnett E C, Najarian M, Majumdar A and Yang P 2008 Enhanced thermoelectric performance of rough silicon nanowires *Nature* **451** 163–8

[5] Nielsch K, Bachmann J, Kimling J and Boettner H 2011 Thermoelectric nanostructures: from physical model systems towards nanograined composites *Adv. Energy Mater.* **1** 713–31

[6] Vineis C J, Shakouri A, Majumdar A and Kanatzidis M C 2010 Nanostructured thermoelectrics: big efficiency gains from small features *Adv. Mater.* **22** 3970–80

[7] Narducci D 2011 Do we really need high thermoelectric figures of merit? A critical appraisal to the power conversion efficiency of thermoelectric materials *Appl. Phys. Lett.* **99** 102104

[8] Song F, Wu L and Liang S 2012 Giant Seebeck coefficient thermoelectric device of MnO_2 powder *Nanotechnology* **23** 085401

[9] Yang Y, Taggart D K, Cheng M H, Hemminger J C and Penner R M 2010 High-throughput measurement of the Seebeck coefficient and the electrical conductivity of lithographically patterned polycrystalline PbTe nanowires *J. Phys. Chem. Lett.* **1** 3004–11

[10] Xu W, Shi Y and Hadim H 2010 The fabrication of thermoelectric $La_{0.95}Sr_{0.05}CoO_3$ nanofibers and Seebeck coefficient measurement *Nanotechnology* **21** 395303

[11] Ohta H *et al* 2007 Giant thermoelectric Seebeck coefficient of a two-dimensional electron gas in $SrTiO_3$ *Nature Mater.* **6** 129–34

[12] Ikeda H and Salleh F 2010 Influence of heavy doping on Seebeck coefficient in silicon-on-insulator *Appl. Phys. Lett.* **96** 012106

[13] Jaworski C M, Kulbachinskii V and Heremans J P 2009 Resonant level formed by tin in Bi_2Te_3 and the enhancement of room-temperature thermoelectric power *Phys. Rev.* B **80** 125208

[14] Vashaee D and Shakouri A 2004 Improved thermoelectric power factor in metal-based superlattices *Phys. Rev. Lett.* **92** 106103

[15] Hicks L D and Dresselhaus M S 1993 Thermoelectric figure of merit of a one-dimensional conductor *Phys. Rev.* B **47** 16631

[16] Mahan G D and Sofo J O 1996 The best thermoelectric *Proc. Natl Acad. Sci. USA* **93** 7436–9

[17] Neophytou N and Kosina H 2011 Effects of confinement and orientation on the thermoelectric power factor of silicon nanowires *Phys. Rev.* B **83** 245305

[18] Zianni X 2010 Diameter-modulated nanowires as candidates for high thermoelectric energy conversion efficiency *Appl. Phys. Lett.* **97** 233106

[19] Kim W, Singer S L, Majumdar A, Vashaee D, Bian Z, Shakouri A, Zeng G, Bowers J E, Zide J M O and Gossard A C 2006 Cross-plane lattice and electronic thermal conductivities of ErAs:InGaAs/InGaAlAs superlattices *Appl. Phys. Lett.* **88** 242107

[20] Narducci D, Selezneva E, Cerofolini G, Romano E, Tonini R and Ottaviani G 2010 Enhanced thermoelectric properties of strongly degenerate polycrystalline silicon upon second phase segregation *Proc. MRS Symp.* **1314** mrsf10-1314-ll05-16

[21] Narducci D, Selezneva E, Cerofolini G, Frabboni S and Ottaviani G 2012 Impact of energy filtering and carrier localization on the thermoelectric properties of granular semiconductors *J. Solid State Chem.* **193** 19

[22] Narducci D, Selezneva E, Cerofolini G, Romano E, Tonini R and Ottaviani G 2010 Opportunities and

challenges in the use of heavily doped polycrystalline silicon as a thermoelectric material. An experimental study *Proc. 8th Europ. Conf. on Thermoelectrics* pp 141–6
[23] Wood C, Chmielewski A and Zoltan D 1988 *Rev. Sci. Instrum.* **59** 951
[24] Scheidemantel T J, Ambrosch-Draxl C, Thonhauser T, Badding J V and Sofo J O 2003 Transport coefficients from first-principles calculations *Phys. Rev.* B **68** 125210
[25] Kim R, Datta S and Lundstrom M S 2009 Influence of dimensionality on thermoelectric device performance *J. Appl. Phys.* **105** 034506
[26] Lundstrom M 2000 *Fundamentals of Carrier Transport* (Cambridge: Cambridge University Press)
[27] Ramu A T, Cassels L E, Hackman N H, Lu H, Zide J M O and Bowels J E 2010 Rigorous calculation of the Seebeck coefficient and mobility of thermoelectric materials *J. Appl. Phys.* **107** 083707
[28] Kosina H and Kaiblinger-Grujin G 1998 Ionized-impurity scattering of majority electrons in silicon *Solid State Electron.* **42** 331–8
[29] Popescu A, Woods L M, Martin J and Nolas G S 2009 Model of transport properties of thermoelectric nanocomposite materials *Phys. Rev.* B **79** 205302
[30] Jacoboni C and Reggiani L 1983 The Monte Carlo method for the solution of charge transport in semiconductors with applications to covalent materials *Rev. Mod. Phys.* **55** 645
[31] www.ioffe.ru/SVA/
[32] Masetti G, Severi M and Solmi S 1983 Modeling of carrier mobility against carrier concentration in arsenic-, phosphorus-, and boron-doped silicon *IEEE Trans. Electron Dev.* **30** 764
[33] Ziman J M 2001 *Electrons and Phonons* (London: Cambridge University Press)
[34] Chantrenne P, Barrat J L, Blase X and Gale J D 2005 An analytical model for the thermal conductivity of silicon nanostructures *J. Appl. Phys.* **97** 104318
[35] Holland M G 1964 Phonon scattering in semiconductors from thermal conductivity studies *Phys. Rev.* **134** A471
[36] Li D, Wu Y, Kim P, Shi L, Yang P and Majumdar A 2003 Thermal conductivity of individual silicon nanowires *Appl. Phys. Lett.* **83** 2934
[37] Moldovan M 2011 Thermal energy transport model for macro-to-nanograin polycrystalline semiconductors *J. Appl. Phys.* **110** 114310
[38] Zebarjadi M, Joshi G, Zhu G, Yu B, Minnich A, Lan Y, Wang X, Dresselhaus M, Ren Z and Chen G 2011 Power factor enhancement by modulation doping in bulk nanocomposites *Nano Lett.* **11** 2225–30
[39] Orton J W and Powell M J 1980 The Hall effect in polycrystalline and powdered semiconductors *Peg. Prog. Phys.* **43** 1263
[40] Seto J Y W 1975 The electrical properties of polycrystalline silicon films *J. Appl. Phys.* **46** 5247
[41] Farmakis F V, Brini J, Kamarinos G, Angelis C T, Dimitriadis C A and Miyasaka M 2001 On-current modeling of large-grain polycrystalline silicon thin-film transistors *IEEE Trans. Electron Dev.* **48** 701
[42] Spadoni S, Acciarri M, Narducci D and Pizzini S 2000 Surface micro-characterisation of silicon wafers by the LBIC technique in planar configuration and by attenuated total reflection spectroscopy *Phil. Mag.* B **80** 579–85
[43] Nishio Y and Hirano T 1997 Improvement of the efficiency of thermoelectric energy conversion by utilizing potential barriers *Japan. J. Appl. Phys.* **36** 170–4
[44] Kim R and Lundstrom M 2011 Computational study of the Seebeck coefficient of one-dimensional composite nano-structures *J. Appl. Phys.* **110** 034511
[45] Lundstrom M 2001 On the mobility versus drain current relation for a nanoscale MOSFET *IEEE Electron Device Lett.* **22** 293–5
[46] Selezneva E, Arcari A, Pernot G, Romano E, Tonini R, Frabboni S, Ottaviani G, Shakouri A and Narducci D 2011 Effect of nanocavities on the thermoelectric properties of polycrystalline silicon *Mater. Res. Soc. Symp. Proc.* **1329** mrss11-1329-i01-09